

High-Quality Transparent Electrodes Spin-Cast from Preformed Antimony-Doped Tin Oxide Nanocrystals for Thin Film Optoelectronics

Li Luo,[†] Deniz Bozyigit,[‡] Vanessa Wood,[‡] and Markus Niederberger^{*,†}

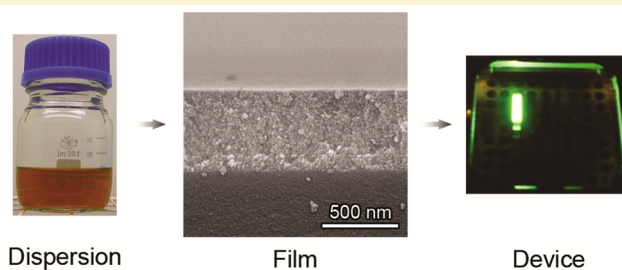
[†]Laboratory for Multifunctional Materials, Department of Materials, ETH Zurich, 8093 Zurich, Switzerland

[‡]Laboratory for Nanoelectronics, Department of Information Technology and Electrical Engineering, ETH Zurich, 8092 Zurich, Switzerland

S Supporting Information

ABSTRACT: We present the wet-chemical deposition of antimony-doped tin oxide (ATO) nanocrystals into films and demonstrate that these films have the required high quality to be used as transparent electrodes in thin film optoelectronic devices. Monodisperse, 3 nm diameter ATO nanocrystals, synthesized by an efficient microwave-assisted nonaqueous sol–gel method, are dispersed in tetrahydrofuran (THF) without any additives and processed into films by spin-coating on glass substrates. After thermal treatment, uniform and crack-free films with a low surface roughness of 1.6 nm and tunable thickness of 30 to 800 nm are obtained. A sheet resistance of 395 Ω /square is achieved for a 480 nm thick ATO film with a high transparency of 90% in the visible light range (380–780 nm). To demonstrate that these films are indeed viable as transparent electrodes, we show that an organic light emitting diode (OLED) fabricated on our nanoparticle-based ATO electrode exhibits an electrical and optical performance comparable to an OLED on a commercially available indium tin oxide (ITO) film.

KEYWORDS: antimony-doped tin oxide (ATO), benzyl alcohol, nonaqueous sol–gel process, microwave chemistry, transparent conducting oxides, thin films, organic light-emitting diode (OLED)



INTRODUCTION

Transparent conducting oxides (TCOs) exhibit high electrical conductivity and optical transmittance in the visible region. This unique combination of properties renders TCOs suitable as electrodes in devices, such as liquid crystal displays (LCDs),¹ light-emitting diodes (LEDs),² solar cells,³ and smart windows.⁴ In addition to electrical conductivity and optical transparency, TCOs for thin film optoelectronic devices must be ultrasmooth and provide a suitable work function⁵ and surface chemistry,⁶ as well as long-term stability⁷ under electrical bias. Currently, the commercially available TCO with the best electrical and optical properties is indium tin oxide (ITO), which is typically deposited by magnetron sputtering. However, indium is a rather expensive metal, and also physical vapor deposition of films is costly due to the high vacuum nature of the technique and the frequent cleaning of the deposition chambers that is required. The rapidly growing demand for consumer electronics, photovoltaics, and smart building materials requires the development of lower cost but equally high performance TCOs.

Next generation transparent conductors (TCs) must use readily available constituent materials and a film processing that is not only compatible with large-scale manufacturing methods but also less expensive.⁸ Solution-processed graphene,⁹ carbon nanotubes,¹⁰ and metal nanowire networks¹¹ have been

proposed as transparent electrodes. Some of these reported carbon-/metal-based TCs performed nearly as good as commercial ITO, and functional devices have been demonstrated as well. However, the transmittance of these nonoxide electrodes is highly dependent on the thickness of the films, and therefore, the development of fabrication processes, especially solution processes, to obtain either homogeneous and very thin film or network structures over large areas is a key point for industrial applications. In this respect, other strategies have to be developed in parallel. Compounds based on tin oxide and zinc oxide, and on the production side, pyrolytic spray and wet-chemical deposition are considered two attractive alternatives. The pyrolytic spray deposition has frequently been used as a low cost method for glass coatings. However, this method often results in irregular surfaces, which are not acceptable for thin film device electrodes.⁷ In the case of wet-chemical deposition, sol–gel chemistry has intensively been studied.¹² However, sol–gel films are typically amorphous, and to induce crystallization, the films have to be heat treated, which often negatively affects the quality of the films through

Received: September 9, 2013

Revised: November 7, 2013

Published: December 4, 2013

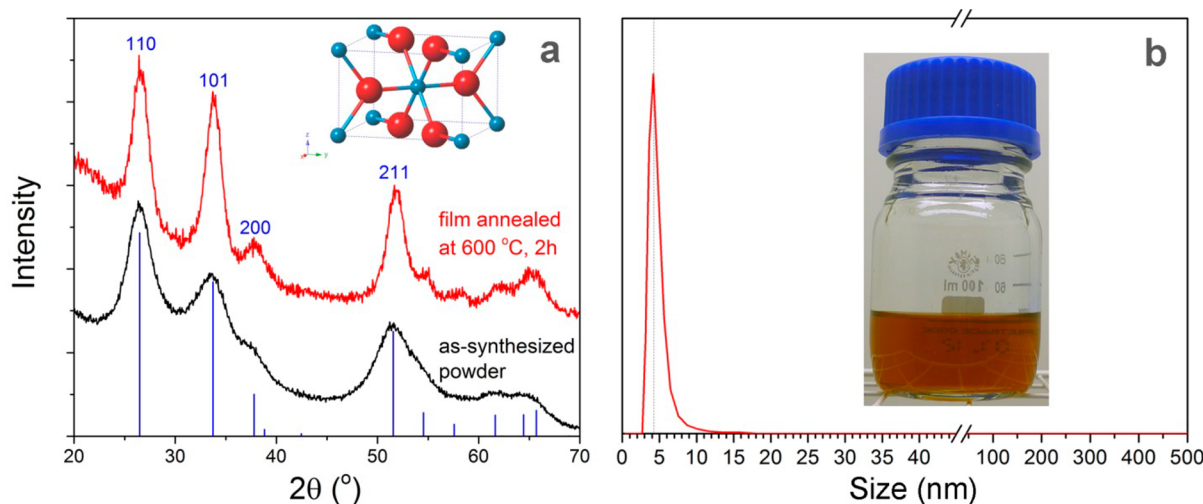


Figure 1. (a) PXRD patterns of as-synthesized ATO powders and of the spin-cast nanocrystal-based film annealed at 600 °C for 2 h and reference PXRD peaks (represented as vertical bars) of SnO_2 cassiterite structure (ICSD PDF no. 77-0452). (b) Size distribution of ATO nanoparticles in THF from DLS measurement. The inset shows a photograph of ATO dispersion in THF with solid concentration of ~ 140 mg/mL.

the formation of cracks, an increase in surface roughness, or phase segregation in the case of doped metal oxides.

For these reasons, in the past few years, great efforts have been put into the processing of nanoparticles into films. The main advantage is that the film deposition is divided into two steps, which can be controlled separately. First, nanoparticles are synthesized to the desired size, shape, and composition. The film deposition involves traditional wet-chemical techniques, performed with simple equipment and under ambient pressure. In addition, the nanoparticle dispersions can be used as inks in industrial processes such as inkjet printing and roll-to-roll production.¹³ Such deposition techniques make it easily possible to control the porosity to increase the surface area.¹⁴

A considerable amount of literature is available on the synthesis of TCO nanocrystals including materials such as ITO,¹³ Al-doped zinc oxide (AZO),¹⁵ and Sb-doped tin oxide (ATO),^{14a,16} and their assembly into films by low-cost methods such as spin- or dip-coating. Although reasonable electrical conductivities and optical transparencies were obtained for ITO and AZO, few devices using these nanoparticle films have been reported due to many other problems. Indium is known to diffuse into the active layers of OLEDs resulting in degradation of performance,¹⁷ and AZO is chemically unstable, making it difficult to obtain the smooth surfaces necessary for thin film devices, such as OLEDs.¹⁵ Therefore, we focused our work on ATO nanoparticles. To date, the electrical conductivity of solution-processed ATO films has only been used in conjunction with ITO or fluorine-doped tin oxide (FTO) electrodes to enhance water electrolysis^{16b,18} or to improve light extraction in the application of LEDs.¹⁹

Here, we describe the preparation of a high performance TCO by the wet-chemical deposition of preformed ATO nanocrystals and its use as an electrode for thin film optoelectronic devices. The ATO nanocrystals are synthesized by a microwave-assisted nonaqueous sol-gel method, a fast and efficient process for metal oxide nanoparticle synthesis.²⁰ These well-dispersed ATO nanocrystals are spin-coated on glass substrates to achieve smooth, highly transparent, and conductive ATO films. An OLED fabricated on this ATO nanocrystal-based TCO film shows device performance that is nearly identical to that of the reference OLED fabricated on

commercial ITO. To our knowledge, this is the first example of a nanocrystal-based TCO, which fulfills the requirements needed for an OLED device.

RESULTS AND DISCUSSION

Synthesis and Characterization of ATO Nanocrystals.

Synthesis of ATO nanocrystals with antimony doping of 10 mol % Sb/(Sb + Sn) follows a recipe from the literature^{16a} extended to a microwave-assisted approach,^{15,20c,21} which shortens the synthesis time by a factor of 8. After microwave heating of the $\text{Sb}(\text{ac})_3$ and SnCl_4 precursors in benzyl alcohol and toluene at 135 °C for 15 min, highly crystalline ATO nanoparticles are obtained, as shown by the powder X-ray diffraction (PXRD) pattern of the as-synthesized powder (Figure 1a). The crystallinity of the nanoparticles is similar to that of ATO nanocrystals obtained by conventional heating at 150 °C for 2 h.^{16a} The ATO nanocrystals exhibit the cassiterite tetragonal structure of SnO_2 . The average crystal size estimated from the (101) peak broadening and Scherrer equation is 3.2 nm. Dynamic light scattering (DLS) measurements confirm that the size distribution is very narrow (from 3 to 8 nm, mainly between 3.6 to 5.6 nm), and also in the larger size range from 100 to 500 nm no larger particles were detected (Figure 1b). Accordingly, it is not surprising that the ATO dispersion (Figure 1b inset) does not produce any precipitates over months. We attribute the slightly larger particle size determined from DLS over that determined by the fitting of the PXRD to surface-attached organics. Indeed, the organic content of the as-synthesized powders dried in air at 60 °C is about 50 wt % according to the thermogravimetric analysis (Figure S2, Supporting Information). The FT-IR spectrum (Figure S1, Supporting Information) of the as-synthesized powders shows many absorption bands in the range of 1000–3700 cm^{-1} . The main peaks can be ascribed to aromatic C=C stretching, C=O stretching, C—Cl bending, C—H bending, and C—O bending vibration, indicating the presence of surface-adsorbed organic molecules. These peaks disappear after the thermal treatment at 600 °C for 2 h, demonstrating that all the organics are completely removed at this temperature.

Preparation and Characterization of the ATO Films.

The ATO nanocrystals are deposited on a glass substrate by

spin-coating of ATO dispersions in THF. The thickness of the films can be adjusted from 30 to 800 nm by varying the concentrations of the dispersions and/or by repeated spins steps (from 1 to 9 times). Figure 2a–c shows the cross-

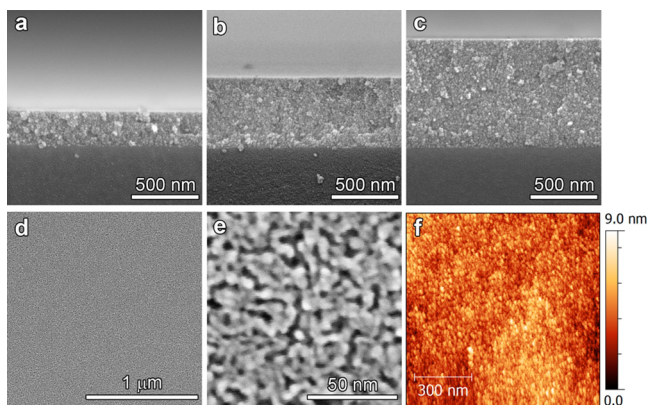


Figure 2. Spin-cast nanocrystal-based ATO films on glass substrates. (a, b, and c) SEM images of the cross-sectional views of ATO films with different thicknesses (from a to c: 260 nm (3 spins), 530 nm (6 spins), 800 nm (9 spins)). The films were annealed in air at 600 °C for 2 h. (d and e) Top view SEM images of an ATO film at different magnifications. (f) AFM image of the same film (rms \approx 1.1 nm).

sectional scanning electron microscope (SEM) images of the ATO films, indicating a stepwise and linear increase of the film thickness by repeated spin-coating. All films appear uniform over the whole substrate (12 \times 12 mm). To remove the residual organics and improve the conductivity, the films are irradiated under UV–vis (260–600 nm) at 43 mW/cm² for 10 h and/or annealed in air at 450–600 °C for 15–120 min. As shown in Figure 1a, the ATO films maintain the cassiterite tetragonal structure of SnO₂ after annealing at 600 °C for 2 h. No second phase is detectable; however, the average crystal size grows from 3.2 to 5.8 nm. This is seen visually in SEM images of the surface of an ATO film annealed at 600 °C for 2 h (Figure 2d,e), which show a smooth, crack-free film composed of wormhole-like pores and a continuous network of particles that are around 6 nm in size. Atomic force microscopy (AFM) of the TCO surface indicates a root-mean square (rms) surface roughness of 1.1 nm (Figure 2f).

More information about the microstructures of as-spin-coated, UV–vis irradiated (at 43 mW/cm² for 10 h) and heat treated (at 600 °C for 2 h) ATO films are obtained using X-ray reflectivity (XRR). Figure 3 shows the specular XRR data for an ATO film after different treatments. Each XRR curve exhibits the classical features of a thin film. Below a critical angle (here, 0.25°), all X-ray photons are reflected (seen as a plateau); at angles above the critical angle, faint interference fringes appear. The critical angle, the slope of the curve, and the period of oscillation enable a calculation of the film thickness, density, and surface roughness. As expected, after UV–vis irradiation and heat treatment, the frequencies of the oscillations become wider, indicating a decrease in film thickness resulting from the removal of residual organics and sintering. Similar densification of nanoparticle films by UV and visible light irradiation on oxide films has been reported before.²² All the XRR data can be fitted based on a two-layer model structure shown in Figure 3 (inset) and in Figure S3 (Supporting Information), where the surface layer refers to the top layer with a thickness of about 2.4 nm and the ATO layer represents the rest of the film

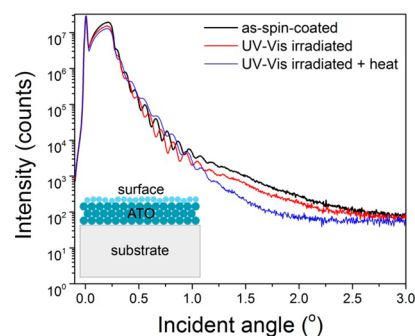


Figure 3. X-ray reflectivity (XRR) data for an ATO film after different treatments: as-spin-coated, UV–vis irradiated at 43 mW/cm² for 10 h, and additionally annealed at 600 °C for 2 h after UV–vis irradiation. The inset: model structure used for XRR data fitting.

underneath. We assume that the surface layer consists of a single layer of disordered and loosely packed ATO nanoparticles, resulting in a lower density in comparison to the rest of the film. This difference in density is reflected in the XRR pattern.

The surface/interface roughness (rms), film thickness, and density of the ATO films after different treatments extracted from the XRR data are summarized in Table S1 (Supporting Information). The surface roughness increases (from 0.264 to 1.661 nm) after UV–vis irradiation and heat treatment due to removing of the adsorbed organics and sintering of the particles, while the surface/ATO interface merges together; i.e., the roughness of the surface/ATO interface drops from 1.284 to 0.529 nm. The overall surface roughness of the film annealed at 600 °C for 2 h is about 1.6 nm, which is in good agreement with the value obtained by AFM (\sim 1.1 nm in an area of 1 μ m²). Whereas the heat treatment leads to a higher density of the surface layer, presumably due to stronger attachment to the layer below, the density of the ATO layer only slightly decreases after UV–vis irradiation and heat treatment. The density of the annealed ATO film (3.27 g/cm³) is much lower than the bulk density of SnO₂ (6.95 g/cm³), indicating a porosity of 52.9%. Although the films get more compact during the UV and heat treatment, a high porosity remains as a consequence of the removal of the large amount of organic residues that basically act as a porogen. After the disappearance of the organics, the nanoparticles are already sintered together and not mobile enough to rearrange into a close packed structure.

Figure 4a–c shows the dependence of electrical resistivity (ρ), the mobility (μ), and the carrier concentration (n) of 53 nm thick films on different annealing temperatures and times determined by Hall Effect measurements. In general, higher annealing temperatures (up to 600 °C) and longer annealing times (up to 2 h) lead to lower electrical resistivity (Figure 4a). However, for temperatures higher than 550 °C, longer annealing times (over 15 min) do not lead to significant improvements of the resistivity. The mobility slightly increases with increasing annealing temperature due to the sintering of the particles (Figure 4b). The carrier concentration does not change remarkably because of the same doping level for all samples (Figure 4c). But for the mobility as well as for the carrier concentration no monotonic trends are visible, which can partly be explained by the difficulty to measure such low mobility values by Hall effect measurements.

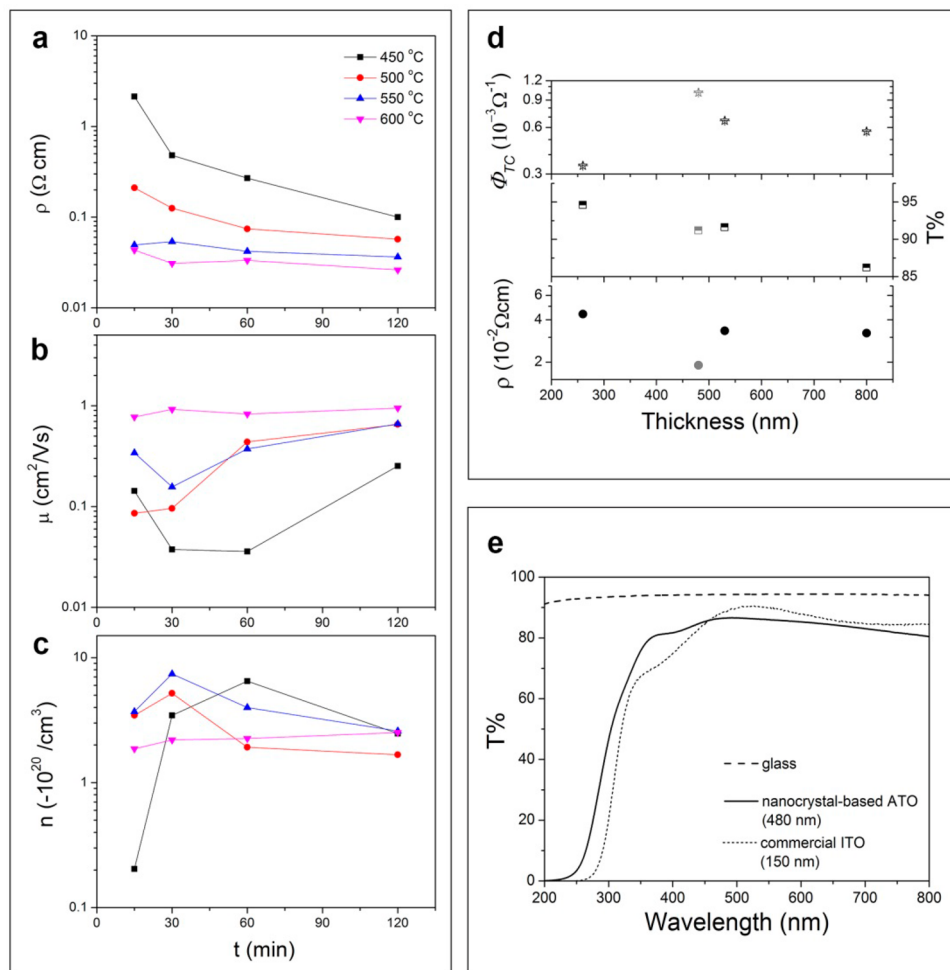


Figure 4. Dependence of (a) the electrical resistivity (ρ), (b) the mobility (μ), and (c) the carrier concentration (n) of the ATO films (with thickness of 53 nm) on the annealing temperature and time. (d) Electrical resistivity (ρ), transmittance (T), and Haacke figure of merit ($\Phi_{TC} = T^{10}/R_{sh}$) of ATO films annealed at 600 °C for 2 h as function of the film thickness. Gray colored data refer to a 480 nm thick film with additional UV-vis irradiation (at 43 mW/cm² for 10 h) before annealing. (e) UV-vis transmittance spectra of a bare glass substrate, nanocrystal-based ATO film of 480 nm thickness, and commercial ITO film with thickness of 150 nm both on glass substrates.

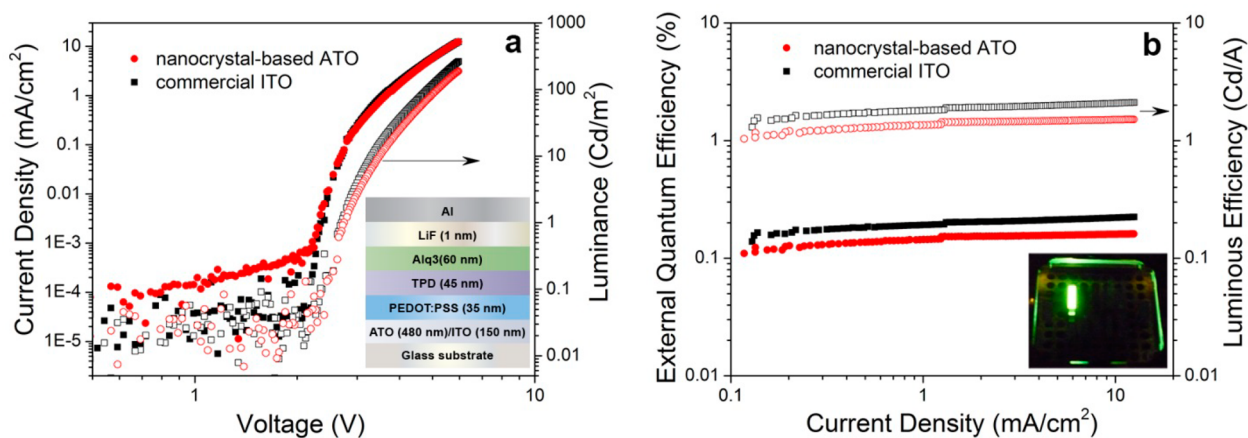


Figure 5. (a) Current density (solid symbols) and luminance (open symbols) versus applied voltage for OLEDs on nanocrystal-based ATO film (circle) and commercial ITO film (square). The inset schematic shows the OLED device structure. (b) External quantum efficiency (EQE) (solid symbols) and luminous efficiency (open symbols) for OLEDs on a nanocrystal-based ATO film (circle) and on a commercial ITO film (square). The inset shows a photograph of a device fabricated from a nanocrystal-based ATO anode operating at 6 V.

The impedance spectra of the same set of samples are also analyzed (Figure S4, Supporting Information). The extracted parallel resistance as a function of annealing temperatures and

times is in excellent agreement with the DC measurements (Figure S4c, Supporting Information). Furthermore, between DC and 1 MHz no significant change in the resistance (Figure

S4b, Supporting Information) is observed, indicating the suitability of our thin films for any number of applications, including those with fast refresh rates.

Figure 4d shows the electrical resistivity (ρ) and transmittance (T) of the ATO films annealed at 600 °C for 2 h as function of the film thickness. As expected, both resistivity and transmittance decrease with increasing the thickness. The thickness of the film is optimized at around 500 nm using Haacke figure of merit ($\Phi_{TC} = T^{10}/R_{sh}$).²³ By applying an additional UV-vis irradiation at 43 mW/cm² for 10 h before annealing, the resistivity decreased from $3.3 \times 10^{-2} \Omega \text{ cm}$ to $1.9 \times 10^{-2} \Omega \text{ cm}$ ($R_{sh} = 395 \Omega/\text{square}$) for a 480-nm-thick film without affecting the transmittance of more than 91% in the green light range. The Haacke figure of merit for this film is calculated to be $1.0 \times 10^{-3} \Omega^{-1}$, which is lower than the one for the commercial ITO ($3.6 \times 10^{-2} \Omega^{-1}$). However, this resistivity is one of the lowest ever reported for nanoparticle-based films, i.e., lower than the recently published resistivity of nanocrystal-based ATO films,²⁴ and only slightly higher than the resistivity of nanocrystal-based ITO films, which hold the conductivity record.^{13b}

Figure 4e shows the optical transmittance spectrum of a nanocrystal-based ATO film. In the visible light range (380–780 nm), the average transmittance of a 480 nm-thick ATO is 84% (with glass substrate), which is comparable to the 85% transmission of a 150 nm thick commercial ITO film. Furthermore, as shown in Figure S5 (Supporting Information), this transmittance of the ATO extends into the near-IR, providing transmittance of over 60% up to 1500 nm (0.82 eV), indicating its suitability for solar cell applications.

Fabrication and Characterization of OLEDs on ATO Electrodes. To demonstrate the potential of these nanocrystal-based ATO films for use as transparent electrodes, we choose to test them as an OLED anode, because OLEDs present some of the most stringent requirements for TCOs. As depicted in the inset of Figure 5a, the most basic OLED structure²⁵ is fabricated on both 480 nm thick ATO nanocrystal films and on commercial 150 nm thick ITO films. Representative current density and luminance versus voltage plots are shown in Figure 5a. The current density versus voltage (J – V) characteristics for spin-cast ATO and commercially obtained ITO anode are nearly identical. Both OLEDs' turn-on voltages were 2.3 V, and they reached a luminance of 264 Cd/m² and 189 Cd/m², respectively, at a current density of 12.5 mA/cm². In Figure 5b, the external quantum efficiency (EQE) and luminous efficiency of both ATO-based and ITO-based OLEDs are shown. While this OLED structure is by no means optimized, the OLED on the nanoparticle ATO film exhibits similar electrical and optical performance to that fabricated in parallel on the commercial ITO film. The inset photograph of a device on nanocrystal-based ATO anode biased at 6 V shows uniform light-emission from the pixel area, providing additional confirmation that the ATO film is smooth and crack-free over a large area.

CONCLUSION

In this work, we prepared high performance TCO films from preformed ATO nanocrystals by wet-chemical deposition. The ATO nanocrystals with sizes of 3 nm were prepared by a fast, microwave-assisted nonaqueous sol–gel route and directly processed into highly stable dispersions in THF with solid concentrations of up to 300 mg/mL. Spin-coating of these dispersions resulted in ATO films with low surface roughness (rms < 1.6 nm), high transparency ($T\% > 90\%$), and good

conductivity ($R_{sh} < 395 \Omega/\text{sq}$). The electrical and optical performance of an OLED fabricated on the ATO nanocrystal film was comparable to that of an OLED fabricated on the commercial ITO film. These results confirm that it is possible to fabricate films from nanocrystal dispersions with sufficiently high quality for use in optoelectronic devices and provide an encouraging pathway to the development of wet-chemical deposition techniques as cost-saving alternatives to high-vacuum processes.

EXPERIMENTAL SECTION

Materials. Sb(III) acetate ($\text{Sb}(\text{ac})_3$) (99.99%), Sn(IV) chloride (SnCl_4) (99%), toluene (anhydrous, 99.8%), benzyl alcohol (99.8%, anhydrous), and tetrahydrofuran ($\geq 99.5\%$) were purchased from Aldrich; and poly(3,4-ethylenedioxythiophene)-poly(styrenesulfonate) (PEDOT:PSS) was purchased from Clevios (P VPCH 8000), N,N' -bis(3-methylphenyl)- N,N' -diphenylbenzidine (TPD) ($>99\%$, EL device grade) from Nichem, tris-(8-hydroxyquinoline)aluminum (Alq3) from Lumtec, lithium fluoride (LiF) (99.99%, metals basis) from Alfa Aesar, Al (99.99%) from Umicore, and Ag (99.999%) from Lesker. All chemicals were used as-received without further purification.

Synthesis of ATO Nanocrystals. ATO nanocrystals were synthesized using a microwave-assisted nonaqueous sol–gel method based on a previous published work.^{16a} In a typical synthesis, 403 mg of $\text{Sb}(\text{ac})_3$ and 1.44 mL of SnCl_4 were added to 10 mL of toluene, and then 30 mL of benzyl alcohol was added under continuous stirring. The mixture was a clear solution. Then, 20 mL of this clear solution was transferred to a 35 mL vessel sealed with a Teflon cap. The reaction mixture was heated by a microwave reactor (CEM Discover) at 135 °C for 15 min with high stirring rate. The precipitate was separated from the liquid phase by centrifugation. The wet powders were dispersed in THF without washing and without any surfactants for film preparation. The solid concentration of the dispersion can be higher than 300 mg/mL.

Film Preparation. A film was prepared on a glass substrate (12 × 12 mm) by spin-coating from the dispersion using a SPIN150 spin-coater. Prior to deposition, the substrates were cleaned by a procedure as follows: sonication in detergent/water solution for 5 min, sonication in distilled water for 5 min twice, sonication in acetone for 2 min twice, sonication in boiling isopropanol for 2 min, and blowing dry with a nitrogen gun.

The spinning speed was set at 6000 rpm for 60 s, and the ramping speed was 7500 rpm/s. After each spin the films were dried in air at 100 °C for 10 min in a preheated furnace. The thickness of the films can be tuned by changing the solid concentration of the dispersion and/or repeating spin. Afterward, the films were annealed in a preheated furnace between 450 and 600 °C for 15–120 min in air, followed by naturally cooling down to room temperature outside of the furnace. Some of the films had an additional UV-vis irradiation (wavelength range in 260–600 nm at 43 mW/cm² for 10 h) before annealing using a honlegrupp UVACUBE 2000 equipped with an F-Strahler lamp.

OLED Fabrication. OLEDs were fabricated in a thermal evaporator (Oerlikon Leybold Vacuum) at a base pressure of around 2×10^{-7} mbar using molybdenum shadow masks to define the device area of 2 mm². Nanocrystal-assembled ATO films and commercially obtained ITO films were cleaned with O₂ plasma. PEDOT:PSS was deposited on the cleaned conducting substrates by spin-coating of a diluted solution (40 vol % DI water) in ambient air at 5000 rpm, followed by curing at 150 °C for 30 min in air. The TPD (45 nm), Alq3 (60 nm), LiF (1 nm), Al (100 nm), and Ag (300 nm) layers were deposited by thermal evaporation. Film thicknesses were monitored using a calibrated quartz crystal sensor. Each cathode rectangle defined one OLED device, with 10 devices per 12 × 12 mm substrate.

Characterization. The powder X-ray diffraction (PXRD) patterns of the nanocrystals and films were measured in Bragg–Brentano mode and in θ – 2θ geometry with Cu K α radiation on a PANalytical X'Pert

Pro equipped with a high temperature chamber (HTK 1200, Anton Paar) using parallel beam. The X-ray reflectivity (XRR) measurements were taken in a specular ω - 2θ geometry with step sizes of $\omega = 0.005^\circ$ on the same diffractometer. XRR data were fitted using X'Pert Reflectivity software (PANalytical).

The microstructure and thickness of the films were characterized using scanning electron microscopy (SEM, Hitachi SU70) equipped with a field emission gun operated at 15 kV in secondary electron imaging mode. The cross sections of the films were sputter-coated with a platinum layer to reduce any charge effect. The surface roughness of the films was characterized by atomic force microscopy (AFM, Agilent 5500) using intermittent contact mode.

Dynamic light scattering (DLS) of ATO dispersion in THF was measured in quartz cuvettes with ZETASIZER (Nano series, Malvern). The infrared spectra of the powders were recorded in a wavenumber range of 375–4000 cm^{-1} using a Bruker ALPHA FT-IR (Fourier transformer infrared) spectrophotometer. The UV–vis transmittance spectra of the films were measured on a JASCO V-660 spectrophotometer. Thermogravimetric analysis (TGA) for the dried powders was performed on a STA 449C Jupiter thermal analysis system (NETZSCH GmbH, Germany). Scans were performed in air at a temperature range of 37–1000 $^\circ\text{C}$ and a rate of 10 $^\circ\text{C}/\text{min}$.

The electrical properties of the films were measured at room temperature using Van der Pauw method on a Hall Effect measurement system (Ecopia HMS-3000) with a 0.55 T magnet kit. The film with a size of 12 \times 12 mm was contacted to a measurement template with gold spring. The complex impedance spectroscopy was carried out by a ZAHNER impedance analyzer using two-point contact in a frequency range from 100 Hz to 4 MHz.

Current–voltage (I – V) characteristics of the OLEDs were measured using a Solartron Modulab MTS in a glovebox under N_2 atmosphere. Luminance was measured using a calibrated flat photodetector (818-UV, Newport Corporation) from the substrate side of the devices.

■ ASSOCIATED CONTENT

■ Supporting Information

FT-IR spectra and TGA and DTA curves for ATO powders; XRR fitting matches and results; impedance data fitting results; and UV–vis–NIR spectra of ATO films. This material is available free of charge via the Internet at <http://pubs.acs.org>.

■ AUTHOR INFORMATION

Corresponding Author

*E-mail: markus.niederberger@mat.ethz.ch.

Author Contributions

L.L. synthesized the nanoparticles, developed the thin film deposition technique, and performed all physical characterization measurements. L.L. and D.B. fabricated and characterized the OLEDs. M.N. and V.W. supervised the project. All authors contributed to the writing of the manuscript. All authors have given approval to the final version of the manuscript.

Notes

The authors declare no competing financial interest.

■ ACKNOWLEDGMENTS

Financial support by ETH Zürich (ETH-0709-2) is gratefully acknowledged. We thank Dr. Dorota Koziej for fruitful discussions regarding the impedance measurement and analysis, Florian Heiligttag for help on FT-IR spectroscopy measurements, and Dr. Barbara Scherrer for the TGA measurement.

■ REFERENCES

- (1) Hilsum, C. *Philos. Trans. R. Soc. A* **2010**, 368 (1914), 1027–1082.
- (2) (a) Wood, V.; Panzer, M. J.; Caruge, J. M.; Halpert, J. E.; Bawendi, M. G.; Bulovic, V. *Nano Lett.* **2010**, 10 (1), 24–29. (b) Wood, V.; Panzer, M. J.; Halpert, J. E.; Caruge, J. M.; Bawendi, M. G.; Bulovic, V. *ACS Nano* **2009**, 3 (11), 3581–3586.
- (3) (a) Pattantyus-Abraham, A. G.; Kramer, I. J.; Barkhouse, A. R.; Wang, X. H.; Konstantatos, G.; Debnath, R.; Levina, L.; Raabe, I.; Nazeeruddin, M. K.; Gratzel, M.; Sargent, E. H. *ACS Nano* **2010**, 4 (6), 3374–3380. (b) Sheel, D. W.; Yates, H. M.; Evans, P.; Dagkaldiran, U.; Gordijn, A.; Finger, F.; Remes, Z.; Vanecek, M. *Thin Solid Films* **2009**, 517 (10), 3061–3065. (c) Beneking, C.; Rech, B.; Wieder, S.; Kluth, O.; Wagner, H.; Frammelsberger, W.; Geyer, R.; Lechner, P.; Rubel, H.; Schade, H. *Thin Solid Films* **1999**, 351 (1–2), 241–246.
- (4) Granqvist, C. G. *Sol. Energy Mater. Sol. Cells* **2007**, 91 (17), 1529–1598.
- (5) (a) Helander, M. G.; Wang, Z. B.; Qiu, J.; Greiner, M. T.; Puzzo, D. P.; Liu, Z. W.; Lu, Z. H. *Science* **2011**, 332 (6032), 944–947. (b) Cao, X. A.; Zhang, Y. Q. *Appl. Phys. Lett.* **2012**, 100 (18), 183304.
- (6) Cui, J.; Wang, A.; Edleman, N. L.; Ni, J.; Lee, P.; Armstrong, N. R.; Marks, T. J. *Adv. Mater.* **2001**, 13 (19), 1476–1480.
- (7) Ginley, D. S. *Handbook of Transparent Conductors*; Springer: New York, 2010.
- (8) Kumar, A.; Zhou, C. W. *ACS Nano* **2010**, 4 (1), 11–14.
- (9) (a) Wu, J. B.; Agrawal, M.; Becerril, H. A.; Bao, Z. N.; Liu, Z. F.; Chen, Y. S.; Peumans, P. *ACS Nano* **2010**, 4 (1), 43–48. (b) Eda, G.; Fanchini, G.; Chhowalla, M. *Nat. Nanotechnol.* **2008**, 3 (5), 270–274. (c) Becerril, H. A.; Mao, J.; Liu, Z.; Stoltenberg, R. M.; Bao, Z.; Chen, Y. *ACS Nano* **2008**, 2 (3), 463–470.
- (10) (a) Barnes, T. M.; Reese, M. O.; Bergeson, J. D.; Larsen, B. A.; Blackburn, J. L.; Beard, M. C.; Bult, J.; van de Lagemaat, J. *Adv. Energy Mater.* **2012**, 2 (3), 353–360. (b) Barnes, T. M.; Bergeson, J. D.; Tenent, R. C.; Larsen, B. A.; Teeter, G.; Jones, K. M.; Blackburn, J. L.; van de Lagemaat, J. *Appl. Phys. Lett.* **2010**, 96, 243309.
- (11) (a) Gaynor, W.; Lee, J. Y.; Peumans, P. *ACS Nano* **2010**, 4 (1), 30–34. (b) Lee, J. Y.; Connor, S. T.; Cui, Y.; Peumans, P. *Nano Lett.* **2008**, 8 (2), 689–692. (c) De, S.; Higgins, T. M.; Lyons, P. E.; Doherty, E. M.; Nirmalraj, P. N.; Blau, W. J.; Boland, J. J.; Coleman, J. N. *ACS Nano* **2009**, 3 (7), 1767–1774. (d) Hu, L. B.; Kim, H. S.; Lee, J. Y.; Peumans, P.; Cui, Y. *ACS Nano* **2010**, 4 (5), 2955–2963.
- (12) (a) Goebbert, C.; Nonninger, R.; Aegeter, M. A.; Schmidt, H. *Thin Solid Films* **1999**, 351 (1–2), 79–84. (b) Koebel, M. M.; Nadargi, D. Y.; Jimenez-Cadena, G.; Romanyuk, Y. E. *ACS Appl. Mater. Interfaces* **2012**, 4 (5), 2464–2473. (c) Lobmann, R. J. P. *J. Sol-Gel Sci. Technol.* **2013**, 66, 120–125. (d) Prodi-Schwab, A.; Luthge, T.; Jahn, R.; Herbig, B.; Lobmann, P. *J. Sol-Gel Sci. Technol.* **2008**, 47 (1), 68–73.
- (13) (a) Buhler, G.; Tholmann, D.; Feldmann, C. *Adv. Mater.* **2007**, 19 (17), 2224–2227. (b) Lee, J.; Lee, S.; Li, G. L.; Petruska, M. A.; Paine, D. C.; Sun, S. H. *J. Am. Chem. Soc.* **2012**, 134 (32), 13410–13414.
- (14) (a) Arsenault, E.; Soheilnia, N.; Ozin, G. A. *ACS Nano* **2011**, 5 (4), 2984–2988. (b) Müller, V.; Rasp, M.; Rathousky, J.; Schutz, B.; Niederberger, M.; Fattakhova-Rohlfing, D. *Small* **2010**, 6 (5), 633–637.
- (15) Luo, L.; Rossell, M. D.; Xie, D.; Erni, R.; Niederberger, M. *ACS Sustainable Chem. Eng.* **2013**, 1 (1), 152–160.
- (16) (a) Müller, V.; Rasp, M.; Stefanic, G.; Ba, J. H.; Günther, S.; Rathousky, J.; Niederberger, M.; Fattakhova-Rohlfing, D. *Chem. Mater.* **2009**, 21 (21), 5229–5236. (b) Peng, Q.; Kalanyan, B.; Hoertz, P. G.; Miller, A.; Kim, D. H.; Hanson, K.; Alibabaei, L.; Liu, J.; Meyer, T. J.; Parsons, G. N.; Glass, J. T. *Nano Lett.* **2013**, 13 (4), 1481–1488.
- (17) Lee, S. T.; Gao, Z. Q.; Hung, L. S. *Appl. Phys. Lett.* **1999**, 75 (10), 1404–1406.
- (18) Moir, J.; Soheilnia, N.; O'Brien, P.; Jelle, A.; Grozea, C. M.; Faulkner, D.; Helander, M. G.; Ozin, G. A. *ACS Nano* **2013**, 7, 4261–4274.
- (19) Puzzo, D. P.; Helander, M. G.; O'Brien, P. G.; Wang, Z. B.; Soheilnia, N.; Kherani, N.; Lu, Z. H.; Ozin, G. A. *Nano Lett.* **2011**, 11 (4), 1457–1462.

- (20) (a) Bilecka, I.; Djerdj, I.; Niederberger, M. *Chem. Commun.* **2008**, No. 7, 886–888. (b) Bilecka, I.; Luo, L.; Djerdj, I.; Rossell, M. D.; Jagodic, M.; Jaglicic, Z.; Masubuchi, Y.; Kikkawa, S.; Niederberger, M. *J. Phys. Chem. C* **2011**, *115* (5), 1484–1495. (c) Bilecka, I.; Niederberger, M. *Nanoscale* **2010**, *2* (8), 1358–1374.
- (21) Niederberger, M.; Garnweitner, G. *Chem.—Eur. J.* **2006**, *12* (28), 7282–7302.
- (22) (a) Bertino, M. F.; Smarsly, B.; Stocco, A.; Stark, A. *Adv. Funct. Mater.* **2009**, *19* (8), 1235–1240. (b) Maksimenko, I.; Wellmann, P. J. *Thin Solid Films* **2011**, *520* (4), 1341–1347.
- (23) Haacke, G. *J. Appl. Phys.* **1976**, *47* (9), 4086–4089.
- (24) Hou, K.; Puzzo, D.; Helander, M. G.; Lo, S. S.; Bonifacio, L. D.; Wang, W. D.; Lu, Z. H.; Scholes, G. D.; Ozin, G. A. *Adv. Mater.* **2009**, *21* (24), 2492–2496.
- (25) Tang, C. W.; Vanslyke, S. A. *Appl. Phys. Lett.* **1987**, *51* (12), 913–915.